

Synthesis of One-Dimensional $\text{Ce}_{1-x}\text{Y}_x\text{O}_{2-x/2}$ ($0 \leq x \leq 1$) Solid Solutions and Their Catalytic Properties: The Role of Oxygen Vacancies

Dan Yang,[†] Lei Wang,[†] Yangzhao Sun,[‡] and Kebin Zhou^{*,†}

College of Chemistry and Chemical Engineering, Graduate University of the Chinese Academy of Sciences, Beijing 100049, People's Republic of China, and Ministry of Environmental Protection of China, Beijing 100035, People's Republic of China

Received: December 29, 2009; Revised Manuscript Received: April 9, 2010

Oxygen vacancy plays a critical role in most enhanced performances of ceria-based materials. In this study, a facile hydrothermal method was developed for the synthesis of one-dimensional rare-earth doped ceria: $\text{Ce}_{1-x}\text{Y}_x\text{O}_{2-x/2}$ ($0 \leq x \leq 1$). The doping concentration could be as high as 90% and the oxygen vacancies therein could be tuned in a wide range. The role of oxygen vacancies on the catalytic properties of these one-dimensional solid solutions had been systematically investigated. It was found that the amounts of the dopant (Y^{3+}) determined the concentration, type, and distribution of oxygen vacancies, which in turn influenced the reducibility and catalytic activity of the solid solutions: in the lightly doped ceria ($x \leq 0.1$), oxygen vacancies formed associates with doped ions and improved the reducibility and catalytic activity of materials; with the dopants increased ($0.1 \leq x \leq 0.5$), microdomains or C-type superstructures generated through the ordering of oxygen vacancies formed and decreased the catalytic activity of the solid solutions gradually; while in the heavily doped ceria, the reactivity of the solid solutions was drastically promoted; then, as the crystal transformed into the C-type structure ($x \geq 0.9$), the solid solutions suffered poor reactivity again. The present finding deepens the understanding of the nature of oxygen vacancies and may further guide the design of highly reactive metal oxide catalytic materials.

Introduction

In conjunction with the advantages of nanotechnology, CeO_2 , one of the most important rare-earth oxides, is finding many applications in the fields of catalysis, sensor technology, and biomedical sciences.^{1–6} The key to the wide use of nanoceria lies in its ease of uptaking and releasing oxygen through repeatable shift between Ce^{3+} and Ce^{4+} , during which process oxygen vacancies are involved. Actually, the presence of oxygen vacancies is critical to most enhanced performances of ceria-based materials. According to Mullins et al., the excess electrons left behind by the removal of neutral oxygen are localized on the empty f states, facilitating the valence change of $\text{Ce}^{4+} \rightarrow \text{Ce}^{3+}$ in an extraordinary efficiency, which drastically modifies the reactivity of ceria.^{6,7} Besides, oxygen vacancies are usually the most active centers on the surface of metal oxides, as they can bind adsorbates more strongly than normal oxide sites and assist in their dissociation.⁸

Therefore, large amounts of work have been devoted to the understanding of the relation between the nature of oxygen vacancies (i.e., size, number, distribution state, etc.) and the functionality of ceria-based materials. It is well-known that the mobility of oxygen ions, which can be achieved through repeated formation and annihilation of oxygen vacancies, is crucial to the catalytic activity of nanoceria. Thus quite a few researchers working on the nature of oxygen vacancies focus their effects on the mobility of oxygen. In particular, Esch et al. discovered that small size surface oxygen vacancies on CeO_2

(111) were immobile at room temperature, but linear clusters of these vacancies formed at higher temperatures.⁹ Recently, we found that these larger oxygen vacancy clusters promoted the reducibility and catalytic activity of nanoceria owing to their facilitating effects on the oxygen mobilities.¹⁰ Besides, it is also found that the activation energy of diffusion for the dilute and dispersive oxygen vacancies in crystal lattice is decreased significantly when they bind to small cations compared with larger ones.¹¹ However, the advantage of the dopant with optimum radius would be weakened as the concentration of oxygen vacancies increased. As depicted by Mori et al., the mobility of oxygen vacancies would be blocked efficiently when they formed ordered microdomains.^{12–14} Apparently, the number, distribution state, and mobility of oxygen vacancies are all closely related and directly bound up with the transport and release of oxygen in materials. Therefore, a systematic study on the nature of oxygen vacancies in the crystal lattice and their influence on the catalytic activity of materials might hold paramount importance in the understanding and designing of catalysts with high activity, which has rarely been reported.

One requisite is to control the oxygen vacancies' concentration in a wide range. As has already been attempted by many research groups, doping trivalent rare-earth oxides in ceria is a good way to achieve high-content oxygen vacancies. Unfortunately, the doping concentration (0–45%) and corresponding oxygen vacancies in the as-obtained solid solutions are always in a restricted scope^{14–20} since a large quantity of dopants would lead to inhomogeneity or even phase-separation in the solid solution $\text{Ce}_{1-x}\text{RE}_x\text{O}_{2-x/2}$, which can be essentially attributed to the disparity of the crystal structures between CeO_2 and the doped rare-earth oxides: CeO_2 is assigned to the face-centered cubic (FCC) structure, while the dopants are always simple cubic or hexagonal systems.²¹ With regard to this, searching for the

* To whom correspondence should be addressed. Phone: 86-10-8825-6677. Fax: 86-10-8825-6092. E-mail: kbzhou@gucas.ac.cn.

[†] College of Chemistry and Chemical Engineering, Graduate University of the Chinese Academy of Sciences.

[‡] Ministry of Environmental Protection of China.

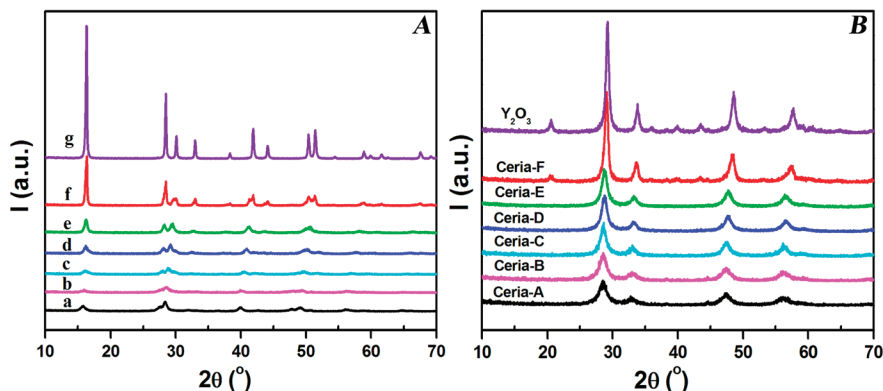


Figure 1. (A) XRD patterns of the hydrothermal products before calcinations: samples for (a) $\text{Ce}(\text{OH})_3$, (b) $\text{Ce}_{0.9}\text{Y}_{0.1}(\text{OH})_3$, (c) $\text{Ce}_{0.7}\text{Y}_{0.3}(\text{OH})_3$, (d) $\text{Ce}_{0.5}\text{Y}_{0.5}(\text{OH})_3$, (e) $\text{Ce}_{0.3}\text{Y}_{0.7}(\text{OH})_3$, (f) $\text{Ce}_{0.1}\text{Y}_{0.9}(\text{OH})_3$, and (g) $\text{Y}(\text{OH})_3$. (B) XRD patterns of the oxide solid solutions: $\text{Ce}_{1-x}\text{Y}_x\text{O}_{2-x/2}$ ($0 \leq x \leq 1$)

dopants of similar crystal structures with the host materials might facilitate the doping process and thus the creation of oxygen vacancies. It is well-known that all the rare-earth hydroxides can be assigned to similar hexagonal structure. Hence it should be much easier to dope Y^{3+} in the $\text{Ce}(\text{OH})_3$, and corresponding uniform oxides $\text{Ce}_{1-x}\text{Y}_x\text{O}_{2-x/2}$ are supposed to be obtained through further dehydration. In the present study, the synthesis of $\text{Ce}_{1-x}\text{Y}_x(\text{OH})_3$ nanorods has been successfully realized by a facile hydrothermal method and the corresponding oxides have been obtained through further calcination. The results showed that the concentration of oxygen vacancies in these solid solutions could be regulated in a wide range since it increased with the concentration of dopants. Moreover, it was found that the state of oxygen vacancies impacted both the mobility of oxygen ions and the stability of crystal structures, which finally led to the variation of the catalytic activity and reducibility of doped ceria.

Experimental Section

Synthesis. All the materials used were of analytical purity. In a typical synthesis, for the molar ratio of $\text{Ce}:\text{Y} = 9:1$, 1 g of CeCl_3 and 0.06 g of YCl_3 were dissolved in the distilled water, and proper amounts of 10% NaOH solution were rapidly added with continuous stirring for about 5 min. Then the obtained slurry was transferred into a 50 mL autoclave, which was filled with deionized water to 80% of the total volume and heated at 120°C for 12 h. The system was then allowed to cool to room temperature. The final product was collected by filtration, washed with deionized water to remove any possible ionic remnants, dried at room temperature for 5 h, and then calcined at 450°C for 5 h. The preparations of other solid solutions of $\text{Ce}_{1-x}\text{Y}_x\text{O}_{2-x/2}$ ($0 \leq x \leq 1$) followed a similar procedure with different molar ratios of the metal precursors and they are denoted as ceria-A, ceria-B, ceria-C, ceria-D, ceria-E, and ceria-F according to the different dopant concentrations: $x = 0, 0.1, 0.3, 0.5, 0.7, 0.9$.

Catalytic Activity Evaluation. The catalytic activities for CO oxidation were evaluated in a fixed-bed quartz tubular reactor. The catalyst particles (0.1 g) were placed in the reactor. The reactant gases 2.0% CO and 16% O_2 , balanced with nitrogen, went through the reactor at a rate of 100 mL/min. The composition of the gas exiting the reactor was monitored by gas chromatography.

Characterization. To check if there were any chloride ions in the synthesized samples, XRF analysis was performed on an EAGLE III spectrometer with the sensitivity of ppm level and no chloride was detected (Figure S1, Supporting Information).

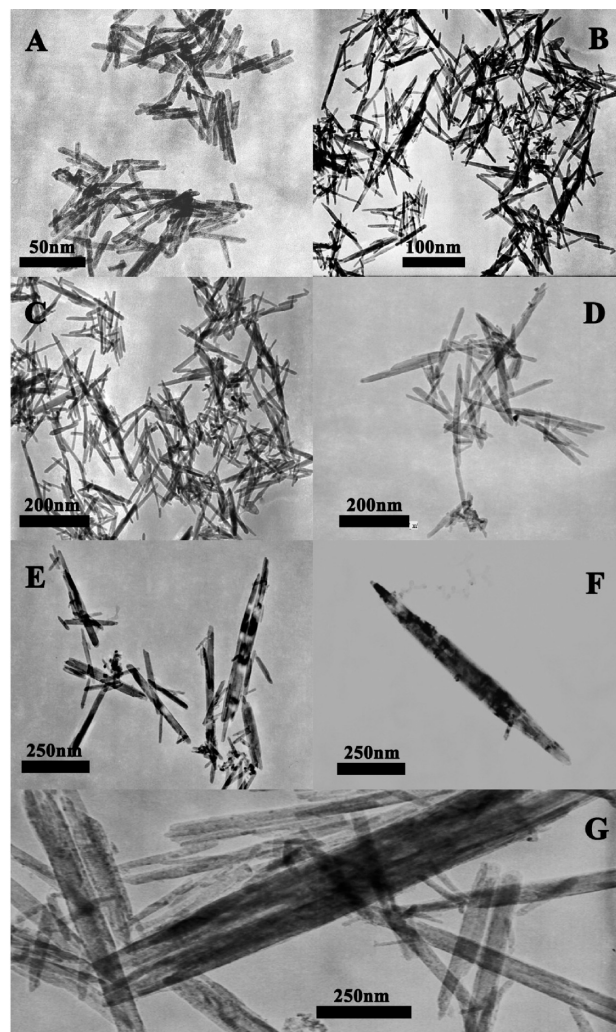


Figure 2. TEM images of the hydroxides before calcinations: (A) $\text{Ce}(\text{OH})_3$, (B) $\text{Ce}_{0.9}\text{Y}_{0.1}(\text{OH})_3$, (C) $\text{Ce}_{0.7}\text{Y}_{0.3}(\text{OH})_3$, (D) $\text{Ce}_{0.5}\text{Y}_{0.5}(\text{OH})_3$, (E) $\text{Ce}_{0.3}\text{Y}_{0.7}(\text{OH})_3$, (F) $\text{Ce}_{0.1}\text{Y}_{0.9}(\text{OH})_3$, and (G) $\text{Y}(\text{OH})_3$.

The size and morphology of all the catalysts were obtained with a JEOL JEM-1200EX transmission electron microscope and a JEM-2010 high-resolution transmission electron microscope. The catalyst powders were dispersed in ethanol to prepare the TEM and HRTEM samples. The X-ray diffraction (XRD) patterns were obtained by using the a Bruker D8 Advance X-ray diffractometer with $\text{Cu K}\alpha$ radiation ($\lambda = 1.5418 \text{ \AA}$). The data were recorded at a scan rate of 2 deg/min. X-ray photoemission

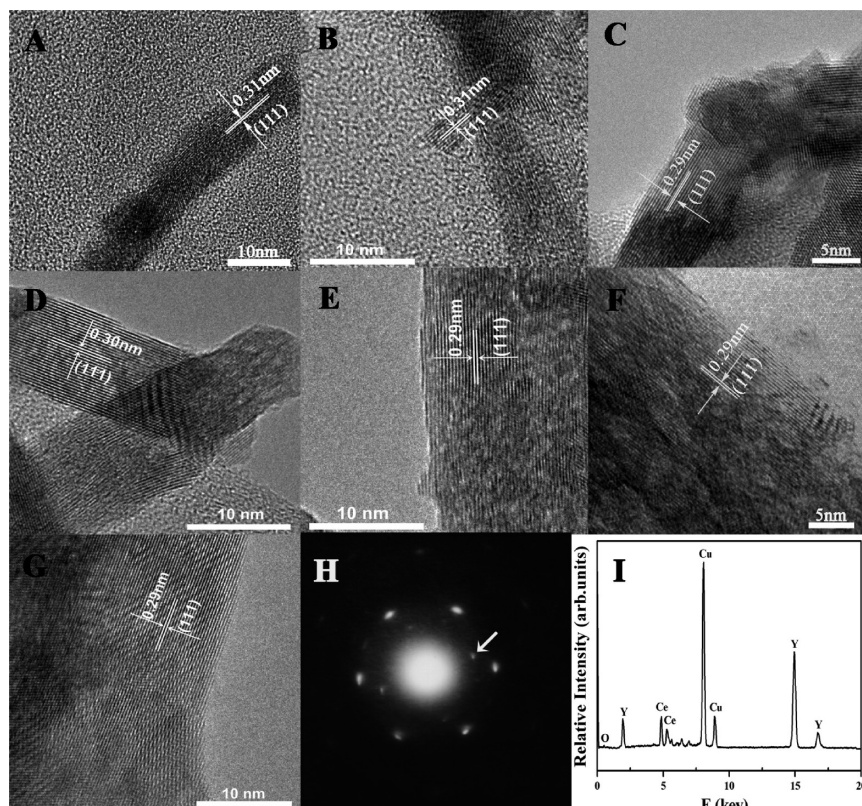


Figure 3. HRTEM images of the oxide solid solutions: (A) ceria-A, (B) ceria-B, (C) ceria-C, (D) ceria-D, (E) ceria-E, (F) ceria-F, and (G) Y_2O_3 . (H) SAED pattern for a single nanorod of ceria-C (the arrow indicates the presence of superstructure (similarly for ceria-D and -E)). (I) EDS spectra for one of the typical nanorods.

spectroscopy (XPS) experiments were carried out in an ESCA Lab220i-XL spectrometer (VG Scientific) with Al $K\alpha$ radiation in twin anode at 14 kV \times 16 Ma, calibrated internally by carbon deposit C (1s) binding energy (BE) at 284.6 eV. The Raman spectra were recorded at room temperature with an XY Dilor spectrograph equipped with a Spex CCD detector (2000 \times 800 pixels). Spectra were recorded in microconfiguration with a laser impact of ca. 1 μm in diameter. The excitation source was the 514.5 nm line of an argon laser at the power level of 5.4 mW. CO temperature-programmed reduction was conducted with a conventional apparatus equipped with a TCD detector. Before the TPR analysis, the samples were treated in pure oxygen at 450 $^\circ\text{C}$ for 45 min. A molecular sieve trap was placed before the detector to adsorb the water produced. TPR was performed by heating the sample (around 70 mg) at 15 deg/min to 950 $^\circ\text{C}$ in a CO–Ar mixture flowing at 40 mL/min. These characterizations of the materials were all carried out after activity evaluation.

Results and Discussion

Crystal Phases and Morphologies of the Solid Solutions.

The precipitants obtained through hydrothermal treatment were dried in air at room temperature for about 5 h and then characterized by powder XRD analysis. As is shown in Figure 1A and Figures S2–S8 (Supporting Information), all the as-synthesized products can be indexed to pure hexagonal structures (typical hydroxide patterns) and the characteristic peaks became sharper and underwent shift toward higher 2θ values with increased concentrations of the dopants, indicating formation of the solid solutions $\text{Ce}_{1-x}\text{Y}_x(\text{OH})_3$ ($0 \leq x \leq 1$). Upon calcination under 450 $^\circ\text{C}$ for 5 h, the corresponding materials were taken for XRD analysis again, as given in Figure 1B, from

which we can see that all the hydroxides had completely dehydrated into oxides. Besides, the products sustained single phase with face-centered cubic (FCC) structures from pure ceria to a certain dopant concentration ($x = 0.7$), confirming the formation of homogeneous oxides solid solutions $\text{Ce}_{1-x}\text{Y}_x\text{O}_{2-x/2}$ and it was not until $x = 0.9$ that the peaks corresponding to the cubic bixbyte structure appeared, manifesting the oxide solid solutions had transformed to the C-type structure.

Figure 2A–G shows the transmission electron microscopy (TEM) images of the hydroxides solid solutions $\text{Ce}_{1-x}\text{Y}_x(\text{OH})_3$ ($0 \leq x \leq 1$). It is clear that all the products exhibited rodlike morphology and their sizes (lengths and diameters) grew uniformly with x , from about 50 to 1500 nm. The morphologies of the calcined oxides remained unchanged and both high resolution transmission electron microscope (HRTEM) and selected area electron diffraction (SAED) (Figure 3) results revealed the single crystalline characteristic of each rodlike particle, which was consistent with our previous studies.¹⁰ Energy dispersive spectra (EDS) analysis was taken on some typical nanorods in order to investigate the composition of these oxides and it was demonstrated that each nanorod was composed of the elements Ce, Y, O (the element Cu was from the substrates), Figure 3I, further confirming the homogeneity of these solid solutions.

The oxidation state of cations in the solid solutions was characterized with X-ray photoelectron spectroscopy (XPS), and trivalent Y ions (Y^{3+}) were easily distinguished in all the doped samples from the asymmetrical peak that could be decomposed to two components at 156.7 and 158.8 eV which were attributed to $\text{Y}3d_{5/2}$ and $\text{Y}3d_{3/2}$, respectively, of Figure 4A, while cerium in all the solid solutions existed in a mixed state of Ce^{3+} and Ce^{4+} ,²² as shown in Figure 4B. To determine the concentration

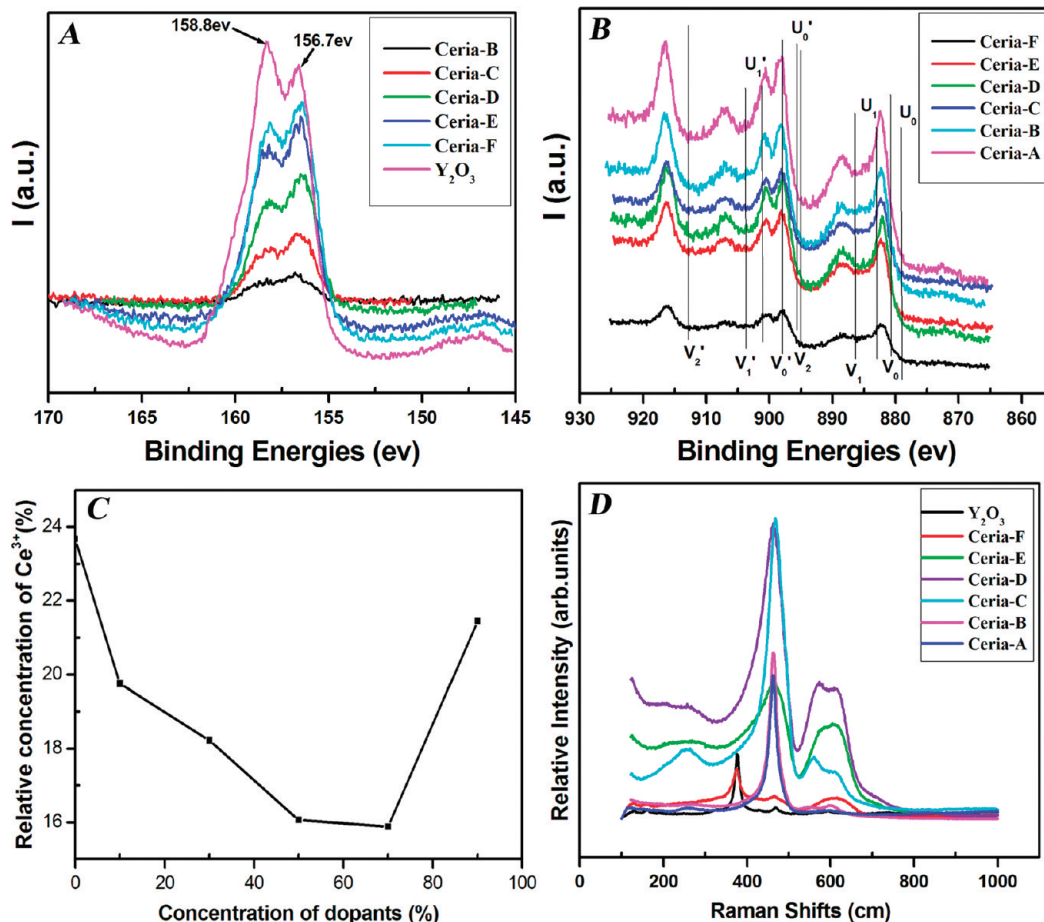


Figure 4. (A) Y_{3d} XPS spectra for $\text{Ce}_{1-x}\text{Y}_x\text{O}_{2-x/2}$ ($0 \leq x \leq 1$). (B) Ce_{3d} XPS spectra for $\text{Ce}_{1-x}\text{Y}_x\text{O}_{2-x/2}$ ($0 \leq x \leq 1$). (C) The relative concentration of Ce^{3+} in the oxide solid solutions. (D) Laser Raman spectra for the oxide products.

of Ce^{3+} and Ce^{4+} , the 3d peak positions were fitted by using PeakFit (Version 4.0) software for the samples. The u_0 , u_1 , and u_1' peaks are characteristic of Ce^{3+} , while v_0 , v_1 , v_2 , v_0' , v_1' , and v_2' are attributed to Ce^{4+} ions. From the ratio of integrated peak areas of Ce^{3+} to the sum of Ce^{3+} and Ce^{4+} , the atomic fraction of Ce^{3+} can be calculated as below:²³

$$[\text{Ce}^{3+}] = \frac{\{A_{u_0} + A_{u_1} + A_{u_1'} + A_{u_0'}\}}{\{A_{v_0} + A_{v_1} + A_{v_2} + A_{v_0'} + A_{v_1'} + A_{v_2'} + A_{u_0} + A_{u_1} + A_{u_1'} + A_{u_0'}\}} \quad (1)$$

where A_i is the integrated area corresponding to peak i , and the calculation results were given in Figure 4C. It can be observed that the relative content of Ce^{3+} in the oxides was decreased upon the increase of doping concentration before $x = 0.7$, which might be caused by the substitution of Y^{3+} for Ce^{3+} that was supposed to present in the fluorite structure. The drastic increase of Ce^{3+} in the solid solutions $\text{Ce}_x\text{Y}_{1-x}\text{O}_{2-x/2}$ ($0.7 < x \leq 1$) was attributed to the reduction of Ce^{4+} in the cubic Y_2O_3 lattice for the electrostatic balance, indicating the structural transformation above $x = 0.9$.

The Mechanism for the Formation of the Solid Solutions.

The solution-based hydrothermal method adopted here is believed to be neither controlled by catalysts nor directed by templates, surfactants, or polymers (template-confined). Hence the morphology evolution and formation of the synthesized solid solutions are directly bound up with the inherent crystal structures, which is the intrinsic ingredient that controls crystal growth and morphologies.²⁴ Although amorphous $\text{Ce}(\text{OH})_3$ and $\text{Y}(\text{OH})_3$ obtained from direct precipitation are insoluble in water

at room temperature and atmospheric pressure, they would gradually dissolve under hydrothermal conditions, which results in atom rearrangement and formation of $\text{Ce}_{1-x}\text{Y}_x(\text{OH})_3$ hydroxides. The generation of such $\text{Ce}_{1-x}\text{Y}_x(\text{OH})_3$ hydroxides was mainly attributed to the isostructural property of the $\text{Ce}(\text{OH})_3$ and $\text{Y}(\text{OH})_3$: they are both hexagonal, $P_{63/m}$, with the metal atoms at 2c (1/3, 2/3, 1/4), and the cation array can be described as linear chains, each of which is surrounded by three other chains and forms hexagonal tunnels where the OH groups are inserted.²¹ It is apparent that the crystal structure is highly anisotropic along the c -axis, which is an important determinant for the morphology of the final product. Therefore, when the concentration of these hydroxides reaches supersaturation, they recrystallize as single crystals with nanorod morphology. After calcining the hydroxides in the air, most of Ce^{3+} in the solid solutions was oxidized into Ce^{4+} while the dopant Y^{3+} remained unchanged since there is no variable valence for the trivalent Y ions. Therefore, in a certain range ($0 \leq x \leq 0.7$), the solid solution maintained the same fluorite structure as the CeO_2 nanocrystal. But when x is above 0.7, as the Ce^{4+} in the lattice was not sufficient enough for the maintenance of fluorite structure, the whole crystal transformed into the cubic bixbyte structure of Y_2O_3 with Ce^{3+} as the doping element for electrostatic balance, as given in the XPS results.

Oxygen Vacancies in the Solid Solutions. It is well-known that once Ce^{3+} or Y^{3+} appears in the fluorite ceria, oxygen vacancies would be generated to maintain the electrostatic balance. Thus, samples were characterized by Laser Raman spectrum to testify the formation of oxygen vacancies, Figure

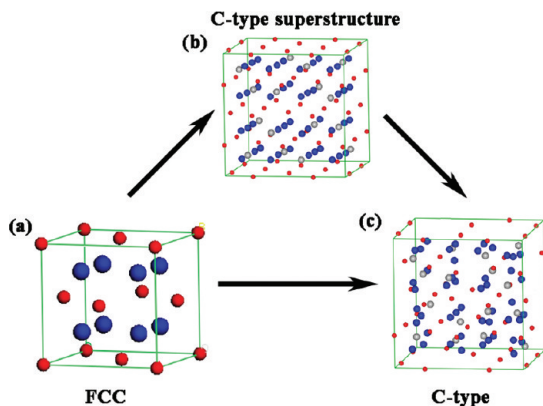


Figure 5. The structural variation upon the doping process: (a) the fluorite structure, (b) the C-type superstructure, and (c) the C-type structure.

4D. It is obvious that pure CeO_2 in the current system exhibited small humps at $\sim 260 \text{ cm}^{-1}$ apart from the sharp first-order Raman peak at $\sim 465 \text{ cm}^{-1}$ due to symmetrical stretching of the Ce–O vibrational unit in 8-fold coordination,²⁵ implying that the CeO_2 sample is not completely defect-free.²⁶ Upon doping with Y^{3+} , two broad, continuously spread, and weak bands at 560 and 600 cm^{-1} also emerged and their intensities kept increasing with the doping concentration before $x = 0.7$.

According to Nakajima et al. the Raman band at $\sim 600 \text{ cm}^{-1}$ is assigned to defect species with Oh symmetry that include a dopant cation in 8-fold coordination of O^{2-} but does not contain any O^{2-} vacancy (MO^{8-} type complex), whereas the Raman bands at 260 and 560 cm^{-1} are attributed to defect species that include an O^{2-} vacancy and have symmetry different from that of the Oh point group.²⁷ Therefore, the firm increase of band intensity at 560 cm^{-1} normalized with 465 cm^{-1} (I_{560}/I_{465}) indicates the continuous increment of oxygen vacancies in the doping range $0.0 \leq x \leq 0.9$.²⁸ Besides, the intensity ratio for the band at 560 and 600 cm^{-1} (denoted as I_{560}/I_{600}) mirrors the relative content of two different kinds of defects in the as-prepared solid solutions,²⁷ as we mentioned above.

Combined with the results reported by Mori et al.,^{16,29,30} the variation process of the dominant defects upon doping ($0 \leq x \leq 1$) can thus be summarized as follows (Figure 5): in the lightly doped ceria ($0 \leq x \leq 0.1$), oxygen vacancies generated mainly formed associates with the highly dispersive substituted trivalent Y^{3+} in FCC structures, given the slight increase of I_{560}/I_{600} ; with more dopants added ($0.1 < x \leq 0.7$), the probability of the cations sitting in close proximity to each other was increased, thus “deep traps” that accommodate all existing mobile oxygen vacancies were generated, and small microdomains would be formed through the ordering of segregated cations and oxygen vacancies in the lattice, which can be justified by the steady

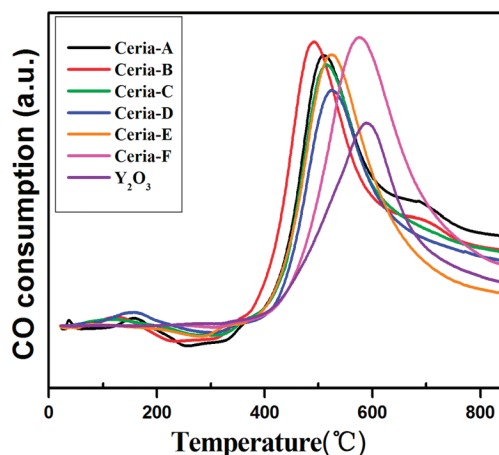


Figure 6. CO-TPR profiles for all the oxide samples.

decrease of I_{560}/I_{600} . Meanwhile, the principal peak at 465 cm^{-1} became highly asymmetric along with its lower energy flank, indicating the FCC structure has been distorted to some extent by these heavily defected structures.²⁶ As the dopants increased, the microdomains developed into a C-type superstructure, in which the fluorite-type structure was modulated with the same periodicity as in the C-type structure and therefore also to be regarded as a commensurately modulated fluorite type.³¹ Figure 3H shows the selected area electron diffraction (SAED) pattern for ceria-C, with the satellite reflections (indicated by the arrow) confirming the presence of C-type superstructure. A clear hump at $\sim 375 \text{ cm}^{-1}$, which was essentially owing to the symmetrical stretching mode of the Y–O vibrational unit in 6-fold coordination, could only be observed at $x = 0.9$. Moreover, there was only a broad peak at $\sim 600 \text{ cm}^{-1}$ resulting from the incorporation of cerium ions in the C-type Y_2O_3 lattice, indicating rare oxygen vacancies were generated at this composition.

For convenience, the main characterization results were summarized in Table 1.

The Reducibility and Catalytic Activity of the Solid Solutions. It is well-documented that the oxygen storage capacity (OSC) and the reducibility are important indicators for the application of ceria as an oxygen transferring component in redox catalysis. Temperature-programmed reduction (TPR) by CO has been used to test the surface and bulk oxygen reducibility of these solid solutions, and the results are shown in Figure 6. All the samples indexed to the FCC structure exhibited a broad reduction profile centered around 500 °C , which is related to the removal of surface oxygen species accompanied by the reduction of surface Ce^{4+} to Ce^{3+} , while that of the C-type crystals was centered at a much higher temperature: 600 °C , indicating FCC structures are more reducible and active than that of C-type. Besides, the reduction

TABLE 1: Summary of the Characterization Data

sample	phase present ^a	BET surface area (m^2/g)	$[\text{Ce}^{3+}]^b$ (%)	rel intensity of typical peaks from Raman spectra			specific rate ($\mu\text{mol m}^{-2} \text{s}^{-1}$)
				I_{560}/I_{465}	I_{600}/I_{465}	I_{600}/I_{560}	
ceria-A	FCC	122.7	23.67				1.3×10^{-2}
ceria-B	FCC	116.5	19.75	0.04	0.03	0.85	1.29×10^{-2}
ceria-C	FCC	87.6	18.22	0.11	0.07	0.66	0.5×10^{-2}
ceria-D	FCC	68.6	16.06	0.38	0.41	1.06	0.01×10^{-2}
ceria-E	FCC	52.3	15.88	0.65	0.71	1.08	1.22×10^{-2}
ceria-F	C	20.9	21.45				0.02×10^{-2}
Y_2O_3	C	10.1					0.01×10^{-2}

^a The X-ray powder diffraction results. ^b The relative concentration of Ce^{3+} derived from the XPS results.

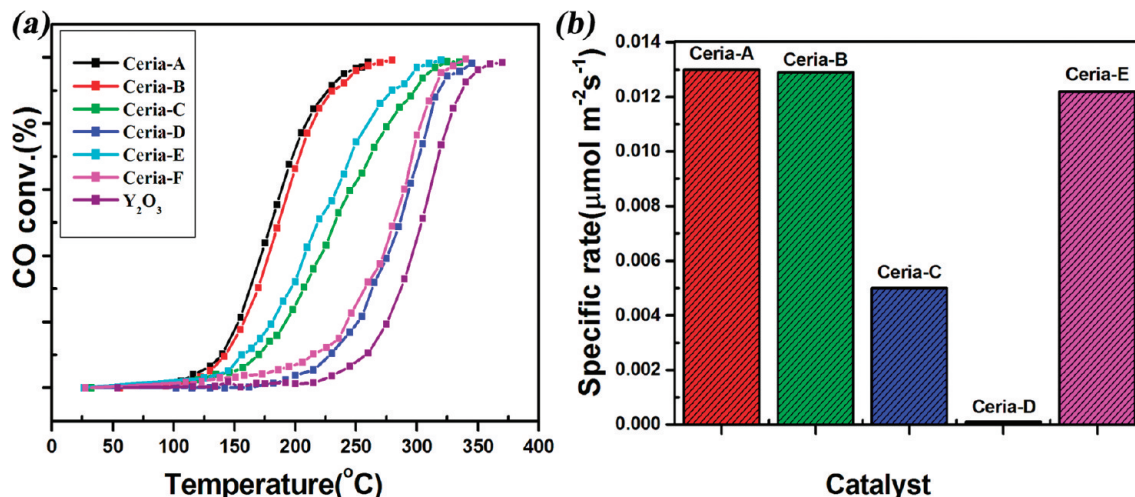


Figure 7. (a) Percentage conversion versus temperature plots for the oxidation of the samples. (b) Graph showing the specific rate for CO oxidation of the FCC solid solutions $\text{Ce}_{1-x}\text{Y}_x\text{O}_{2-x/2}$ ($0 \leq x \leq 0.7$).

peak signifies the amount of available surface oxygen species that can be released and quantitative evaluations of the reactive oxygen species on those FCC-type solid solutions ceria (A–E) were carried out. Obviously, the available active oxygen species were correlated with the concentration of the dopants: light doping ($x \leq 0.1$) promoted the reducibility of ceria nanocrystals, but this facilitating effect was hindered upon continuous addition of doped ions in a certain range ($0.1 < x < 0.7$); then, above a certain concentration ($x = 0.7$), the solid solution acquired excellent reducibility again. Furthermore, the variable reducibility of ceria nanocrystals upon doping different concentrations of Y^{3+} suggests their catalytic activities may be “tuned” via the concentration of dopants. Thus the catalytic activities of these solid solutions were evaluated and the results are given in Figure 7. Not surprisingly, the C-type crystals showed poor activities toward catalytically oxidizing CO, while for the FCC solid solutions, their reactivities behaved in an interesting manner that was consistent with the CO-TPR results: the CO conversion percentage at certain temperatures (175 °C) was decreased continuously with the doping concentration and it was almost zero for ceria-D ($x = 0.5$). Then a drastic increase emerged when it came to ceria-E ($x = 0.7$): the conversion percentage soared to 20%. The corresponding conversion rates of CO (Figure 7b) demonstrated more clearly the regained high reactivity of ceria-E.

Figuring out these extraordinary behaviors needs further explorations on the state of oxygen vacancies and corresponding crystal structures of the solid solutions. As revealed by the Raman spectra, in the lightly doped ceria ($x \leq 0.1$), the substituted trivalent Y^{3+} in FCC structures were highly dispersive and formed associates with oxygen vacancies (small amount) thus generated, which in turn promoted the oxygen vacancy diffusion owing to the attraction between the cations and oxygen vacancies and finally improved the reducibility and catalytic activity of materials. With the dopants increased, according to Mori et al.,^{12–14} the oxygen vacancies thus generated would be rearranged to form ordered microdomains or C-type superstructures, which efficiently blocked the mobility of oxygen vacancies and hence decreased the reactivity of materials. With regard to this, it is no wonder that the reducibility and reactivity of the solid solutions underwent a steady decrease for ceria-C and -D.

Then, why does ceria-E which still contained superstructure gain its activity back? Actually, ceria-E falls into a very special

composition range (with 60–0 mol % $\text{YO}_{1.5}$) of the solutions. A mixture of FCC and C phase, i.e. diphasic, was often observed in such a region.^{31,32} However, in the present work, the single-phase characteristic of ceria-E was revealed by XRD and HRTEM. Such a unique phase feature was also reported by Kimmel et al.³³ For whatever reason, the region around 70 mol % is rather special and sensitive. According to Gabbitas et al.,³² there were strains within the oxygen sublattice when the sample composition was around this region which would in turn lead to an unstable crystal structure of the corresponding samples. Moreover, the calculation results also revealed that the single phase solid solution was at a relative high-energy status in this region.^{34,35} It is rational that the unstable crystal structure would facilitate the transport of oxygen, which was confirmed by the TPR results. Thus, the high activity of ceria-E should be attributed to its highly unstable crystal structure. For $x > 0.7$, once the C-type structure formed, the energy underwent a drastic fluctuation from the maximum to a much lower level. Therefore, the reactivity was significantly enhanced at $x = 0.7$, while the C-type solid solution above this composition showed poor reactivity.

Conclusion

In conclusion, a facile hydrothermal method for the synthesis of one-dimensional $\text{Ce}_{1-x}\text{Y}_x\text{O}_{2-x/2}$ solid solutions through which the dopant concentration can be as high as 90% has been developed successfully. Taking advantage of this system, we studied the relation between the nature of oxygen vacancies and the catalytic activities of ceria-based materials. It was found that the amounts of the dopant (Y^{3+}) determined the concentration, type, and distribution of oxygen vacancies, which in turn influenced the reducibility and catalytic activity of the solid solutions. This work might facilitate the thorough understanding of the nature of oxygen vacancies and their influence on the properties of ceria-based materials and we hope that this finding and novel synthesis route for the one-dimensional rare-earth doped ceria developed here may further guide the design of highly reactive metal oxide catalytic materials.

Acknowledgment. This work was supported by the National Natural Science Foundation of China (20703065, 20877097) and the Ministry of Science and Technology of China (2008AA06Z324).

Supporting Information Available: XRF result for pure ceria and refined XRD patterns for all samples. This material is available free of charge via the Internet at <http://pubs.acs.org>.

References and Notes

- (1) Park, S. D.; Vohs, J. M.; Gorte, R. J. *Nature* **2000**, *404*, 265.
- (2) Fu, Q.; Saltsburg, H.; Flytzani-Stephanopoulos, M. *Science* **2003**, *301*, 935.
- (3) Tarnuzzer, R. W.; Colon, J.; Patil, S.; Seal, S. *Nano Lett.* **2005**, *5*, 2573.
- (4) Fernandez-Garcia, M.; Martinez-Arias, A.; Hanson, J. C.; Rodriguez, J. A. *Chem. Rev.* **2004**, *104*, 4063.
- (5) Andersson, D. A.; Simak, S. I.; Skorodumova, N. V.; Abrikosov, I. A.; Johansson, B. *Proc. Natl. Acad. Sci. U.S.A.* **2006**, *103*, 3518.
- (6) Mullins, D. R.; Overbury, S. H.; Huntley, D. R. *Surf. Sci.* **1998**, *409*, 307.
- (7) Wu, L. J.; Wiesmann, H. J.; Moodenbaugh, A. R.; Klie, R. F.; Zhu, Y. M.; Welch, D. O.; Suenaga, M. *Phys. Rev. B* **2004**, *69*, 125415.
- (8) Pu, Z. Y.; Liu, X. S.; Jia, A. P.; Xie, Y. L.; Lu, J. Q.; Luo, M. F. *J. Phys. Chem. C* **2008**, *112*, 15045.
- (9) Esch, F.; Fabris, S.; Zhou, L.; Montini, T.; Africh, C.; Fornasiero, P.; Comelli, G.; Rosei, R. *Science* **2005**, *309*, 752.
- (10) Liu, X. W.; Zhou, K. B.; Wang, L.; Wang, B. Y.; Li, Y. D. *J. Am. Chem. Soc.* **2009**, *131*, 3140.
- (11) Nakayama, M.; Martin, M. *Phys. Chem. Chem. Phys.* **2009**, *11*, 3241.
- (12) Mori, T.; Drennan, J.; Lee, J. H.; Li, J. G.; Ikegami, T. *Solid State Ionics* **2002**, *154*, 461.
- (13) Mori, T.; Wang, Y. R.; Drennan, J.; Auchterlonie, G.; Li, J. G.; Ikegami, T. *Solid State Ionics* **2004**, *175*, 641.
- (14) Mori, T.; Drennan, J.; Wang, Y.; Auchterlonie, G.; Li, J.-G.; Yago, A. *Sci. Technol. Adv. Mater.* **2003**, *4*, 213.
- (15) Ruiz-Trejo, E.; Maier, J. *J. Electrochem. Soc.* **2007**, *154*, B583.
- (16) Ou, D. R.; Mori, T.; Ye, F.; Kobayashi, T.; Zou, J.; Auchterlonie, G.; Drennan, J. *Appl. Phys. Lett.* **2006**, *89*, 171911.
- (17) Tobash, P. H.; Lins, D.; Bobev, S.; Hur, N.; Thompson, J. D.; Sarrao, J. L. *Inorg. Chem.* **2006**, *45*, 7286.
- (18) Chen, W. Q.; Navrotsky, A. *J. Mater. Res.* **2006**, *21*, 3242.
- (19) Li, G. R.; Qu, D. L.; Arurault, L.; Tong, Y. X. *J. Phys. Chem. C* **2009**, *113*, 1235.
- (20) Wang, Z.; Quan, Z.; Lin, J. *Inorg. Chem.* **2007**, *46*, 5237.
- (21) Vegas, A.; Isea, R. *Acta Crystallogr., Sect. B: Struct. Sci.* **1998**, *54*, 732.
- (22) Qiu, L. M.; Liu, F.; Zhao, L. Z.; Ma, Y.; Yao, J. N. *Appl. Surf. Sci.* **2006**, *252*, 4931.
- (23) Hierro, J.; Sel, O.; Ringuede, A.; Laberty-Robert, C.; Bianchi, L.; Grosso, D.; Sanchez, C. *Chem. Mater.* **2009**, *21*, 2184.
- (24) Tang, Q.; Zhou, W. J.; Zhang, W.; Ou, S. M.; Jiang, K.; Yu, W. C.; Qian, Y. T. *Cryst. Growth Des.* **2005**, *5*, 147.
- (25) Kosacki, I.; Suzuki, T.; Anderson, H. U.; Colomban, P. *Solid State Ionics* **2002**, *149*, 99.
- (26) Mandal, B. P.; Roy, M.; Grover, V.; Tyagi, A. K. *J. Appl. Phys.* **2008**, *103*, 033506.
- (27) Nakajima, A.; Yoshihara, A.; Ishigame, M. *Phys. Rev. B* **1994**, *50*, 13297.
- (28) McBride, J. R.; Hass, K. C.; Poindexter, B. D.; Weber, W. H. *J. Appl. Phys.* **1994**, *76*, 2435.
- (29) Ye, F.; Mori, T.; Ou, D. R.; Cormack, A. N.; Lewis, R. J.; Drennan, J. *Solid State Ionics* **2008**, *179*, 1962.
- (30) Ou, D. R.; Mori, T.; Ye, F.; Zou, J.; Auchterlonie, G.; Drennan, J. *Phys. Rev. B* **2008**, *77*, 024108.
- (31) Wallenberg, R.; Withers, R.; Bevan, D. J. M.; Thompson, J. G.; Barlow, P.; Hyde, B. G. *J. Less-Common Met.* **1989**, *156*, 1.
- (32) Gabbitas, N.; Thompson, J. G.; Withers, R. L. *J. Solid State Chem.* **1995**, *115*, 23.
- (33) Kimmel, G.; Zabicky, J.; Goncharov, E. *J. Alloys Compd.* **2006**, *423*, 102.
- (34) Navrotsky, A.; Simoncic, P.; Yokokawa, H. *Faraday Discuss.* **2007**, *134*, 171.
- (35) Djurovic, D.; Zinkevich, M.; Aldinger, F. *Solid State Ionics* **2008**, *179*, 1902.

JP912227P